

Reversible Tuning of Superconductivity in Ion-Gated NbN Ultrathin Films by Self-Encapsulation with a High- κ Dielectric Layer

Erik Piatti,^{1,*} Marco Colangelo,^{2,*} Mattia Bartoli,^{3,4} Owen Medeiros,²
Renato S. Gonnelli,¹ Karl K. Berggren,² and Dario Daghero^{1,†}

¹*Department of Applied Science and Technology, Politecnico di Torino, I-10129 Torino, Italy*

²*Department of Electrical Engineering and Computer Science,
Massachusetts Institute of Technology, Cambridge, MA 02139, USA*

³*Center for Sustainable Future Technologies-CSFT@POLITO, I-10144 Torino, Italy*

⁴*Consorzio Interuniversitario Nazionale per la Scienza e Tecnologia dei Materiali (INSTM), I-850121 Firenze, Italy*

Ionic gating is a powerful technique for tuning the physical properties of a material via electric-field-induced charge doping, but is prone to introduce extrinsic disorder and undesired electrochemical modifications in the gated material beyond pure electrostatics. Conversely, reversible, volatile, and electrostatic modulation is pivotal in the reliable design and operation of novel device concepts enabled by the ultrahigh induced charge densities attainable via ionic gating. Here we demonstrate a simple and effective method to achieve reversible and volatile gating of surface-sensitive ultrathin niobium nitride films via controlled oxidation of their surface. The resulting niobium oxide encapsulation layer exhibits a capacitance comparable to that of nonencapsulated ionic transistors, withstands gate voltages beyond the electrochemical stability window of the gate electrolyte, and enables a fully reversible tunability of both the normal-state resistivity and the superconducting transition temperature of the encapsulated films. Our approach should be transferable to other materials and device geometries where more standard encapsulation techniques are not readily applicable.

Cite this article as: E. Piatti, M. Colangelo, M. Bartoli, O. Medeiros, R. S. Gonnelli, K. K. Berggren, and D. Daghero. *Phys. Rev. Applied* **18**, 054023 (2022).

I. INTRODUCTION

The ionic gating technique is a very powerful tool to tune the properties of a large variety of materials, including high-carrier density systems such as metals [1–6], BCS superconductors [7–11], thin flakes of metallic transition-metal dichalcogenides [12–14] and iron-based superconductors [15–21] using a field-effect transistor (FET) configuration. In principle, the basic mechanism by which it operates is electrostatic and fully reversible: when the interface between an electrolyte and the material under study is polarized by a gate voltage, the mobile ions accumulate in the so-called electric double layer (EDL) and build up electric fields up to ~ 100 times larger than those achievable in standard solid-dielectric FETs [22, 23]. In practice, however, many processes beyond pure electrostatics can occur in an EDL-FET. These range from the introduction of extrinsic disorder in the form of charged-scattering centers [21, 24–32], to field-induced distortions in the crystal lattice [33–35], to the intercalation of alkali ions [36–46] or protons [47–54], to the outright electrochemical modification of the gated material [16, 33, 34, 55–62]. While these additional processes can be harnessed to provide additional degrees of freedom in modulating the properties of a material, it is often desirable to ensure that the modulation occurs only in the electrostatic regime. Indeed, reversible electrostatic switching is crucial for the realization of novel device concepts, such as chiral-light emitting

transistors [63], superconducting (SC) FETs [64, 65], nanoconstriction Josephson junctions [66, 67] and metallic SC quantum interference devices [68], as well as for reliable operation of stretchable and flexible devices [69–71] and thermoelectric energy harvesters [72].

The most straightforward way to ensure that the operation of an EDL-FET is dominated by reversible charge doping and that electrochemical interactions are suppressed, is to physically separate the active material from the electrolyte using an electrically insulating and electrochemically inert layer. This can be achieved by employing an electrolyte that partially decomposes when polarized, creating a passivation layer [21], but this strongly reduces the switching speed of the device [21]. Another possibility is to employ encapsulation techniques widely used to protect unstable or reactive 2D materials in standard solid-state FETs [73]. For example, one can cover the surface of the active materials, prior to the exposition to the electrolyte, with a high-quality ultrathin layered insulator obtained by micro-mechanical exfoliation of a bulk crystal [13, 14, 24], or a protective dielectric layer [39, 74]. These alternatives, however, can present drawbacks when used in an ionic-gating setup. For instance, the first approach is not easily scalable to multiple integrated devices and large-area geometries [13, 14, 24]. In the second approach, the thickness of the protective layer is critical: thick passivation films strongly suppress the gate capacitance [39, 74], while thin uniform films cannot be deposited on several materials of interest [74]. The development of an alternative, complementary encapsulation technique is therefore highly desirable. In this work, we demonstrate that growth of an ultrathin high- κ dielec-

* These authors contributed equally.

† dario.daghero@polito.it

tric layer on top of a surface-sensitive SC film by means of controlled in-situ oxidation ensures a fully reversible operation of the EDL-FET, a sizeable gate capacitance, a large induced charge-carrier density, and an enhanced tunability of the SC transition temperature with respect to the literature.

II. DEVICE FABRICATION

Our device consists of a niobium nitride multiple-Hall-Bar structure. A 5 nm-thick niobium nitride (NbN) layer was deposited [75] on a 300 nm-thick thermal oxide layer on silicon. The NbN layer was patterned into a multiple-Hall-Bar geometry (see Fig. 1) with direct writing photolithography followed by reactive ion etching. To facilitate the electrical contact with the measurements wires, gold pads were patterned and deposited on the outer lead regions of the Hall bar. The device was then annealed in oxygen atmosphere to grow a Nb₂O₅ insulating barrier via direct oxidation of the superconducting layer. The thickness of the oxide barrier was ≈ 2.6 nm, measured with ellipsometry [76]. More details on the fabrication process are available in the Supplemental Section I [77].

To characterize the device, we defined two measurement channels. The active (gated) channel is created by drop-casting the standard diethylmethyl (2-methoxyethyl) ammonium bis(trifluoromethylsulfonyl)imide (DEME-TFSI) ionic liquid on one section of the Hall bar and on the gate counterelectrode, made of a thin Au flake. The reference (ungated) channel is one of the other sections of the Hall bar, where no ionic liquid was casted. The droplet of liquid on the gated channel is covered with a thin (10 μ m) kapton foil to tightly confine its coverage on the substrate and improve its thermo-mechanical stability.

III. GATE-DEPENDENT ELECTRIC TRANSPORT

Transport measurements were performed in the high-vacuum chamber of a Cryomech[®] pulse-tube cryocooler by the four-wire method after the device was allowed to degas in vacuum at room temperature for at least 1 day to minimize the water absorbed in the electrolyte. A small DC current (I_{DS}) of 1 μ A was injected between the drain and source contacts with the first channel of an Agilent B2912 source-measure unit (SMU), and the voltage drops across the gated (V_{gated}) and reference (V_{ref}) channels were measured with two Agilent 34420 nanovoltmeters to determine the corresponding sheet resistances (R_s). Common-mode offsets such as thermoelectric voltages along the leads and contributions from the gate current were removed via the current-reversal method. The gate voltage (V_G) and current (I_G) were applied and measured between the gate and source contacts with the second channel of the same Agilent SMU. All the temperature (T)-dependent measurements were acquired during the

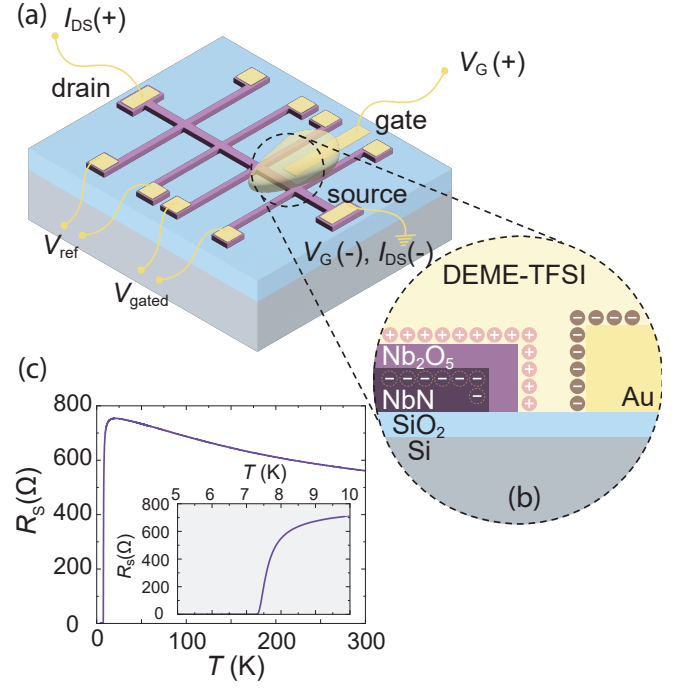


FIG. 1. (a) Sketch of the multiple-Hall-bar structure and of the measurement configuration. Each channel is 1.15 mm long and 100 μ m wide. The typical size of the Au side gate is 0.8×1.2 mm². The ionic liquid droplet is drop-casted so as to cover the Au gate and the gated channel only. (b) Sketch of the cross-section of the gated channel. (c) Sheet resistance R_s as a function of temperature T of the reference channel. Inset shows a magnification around the superconducting transition.

slow, quasi-static warm-up of the devices to room T .

We first assessed the gate-dependent electric transport in our EDL-FETs through the Nb₂O₅ encapsulation layer by sweeping V_G in a triangular wave at $T = 220$ K and monitoring the modulation of the sheet resistance R_s (Fig. 2a). Consistently with what we observed in thick, non-encapsulated films [9, 10], applying a positive V_G (electron doping) reduces the value of R_s , while applying a negative V_G (hole doping) increases it. After completing each sweep, R_s returns to its original value (Fig. S1) irrespectively of the sweep rate within the uncertainty of the measurement [77]. The leakage current I_G was always orders of magnitude smaller than I_{DS} . The tunability of R_s decreases upon increasing the sweep rate, indicating that the relaxation time of the gate loop is dominated by the large resistance of the bulk ionic liquid due to the side-gate configuration [21, 78]. We thus investigated the tunability of R_s over long time scales by applying and removing V_G in a step-like fashion and waiting for the ion dynamics to settle (Fig. 2b). The total modulation of R_s was found to be similar to that due to the triangular wave at the slowest sweep rate 5 mV/s. Most importantly, the modulation was completely reversible upon applying $V_G = 0$ over a comparable time scale to that required for the saturation of R_s upon application of a finite V_G . This

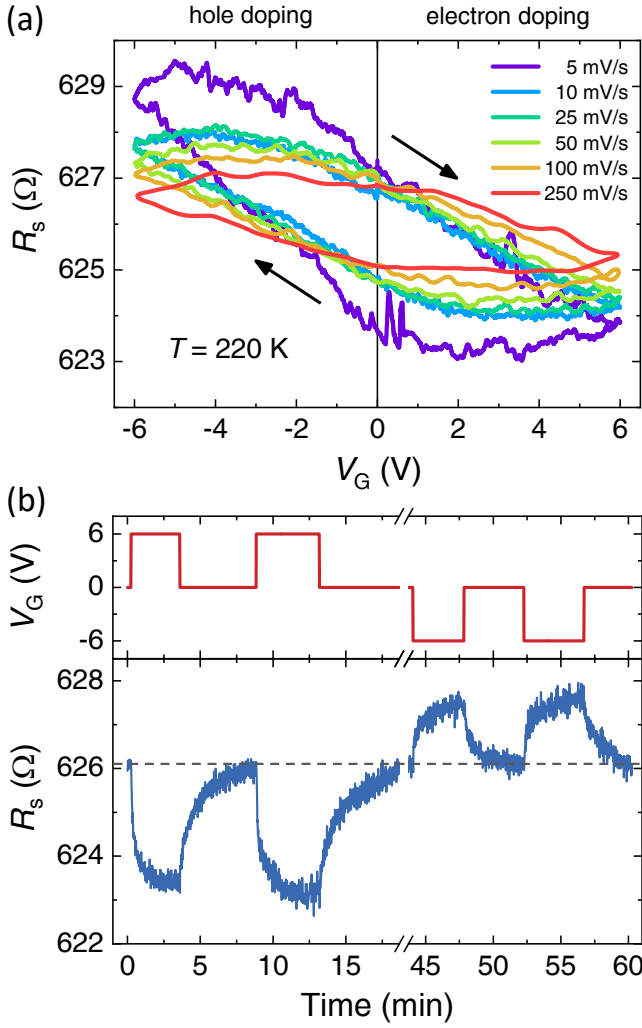


FIG. 2. (a) Sheet resistance R_s as a function of the gate voltage V_G applied as a triangular wave at $T = 220$ K, for different values of the sweep rate. (b) Typical response of R_s (blue line, bottom panel) to the step-like application and removal of positive and negative values of V_G (red line, top panel) at $T = 220$ K. Dashed line is a guide to the eye.

complete reversibility was observed for both positive and negative applied V_G in the Nb_2O_5 -encapsulated devices, which is the typical feature of a modulation occurring via pure charge doping [1, 2, 21, 30]. Note that these reversible modulations of R_s were retained when the devices were then cooled below the freezing point of the ionic liquid with a finite V_G applied (Fig. S2 [77]), further excluding the possibility that they might be an artifact due to a finite (even if small) gate leakage. Conversely, control measurements performed on non-encapsulated ultrathin NbN films resulted in modulations of R_s which were largely irreversible upon V_G removal (Fig. S3 [77]). This finding is in agreement with our earlier results on non-encapsulated films when their thickness was reduced below ~ 10 nm [10].

We gain further insight on the gate modulation process

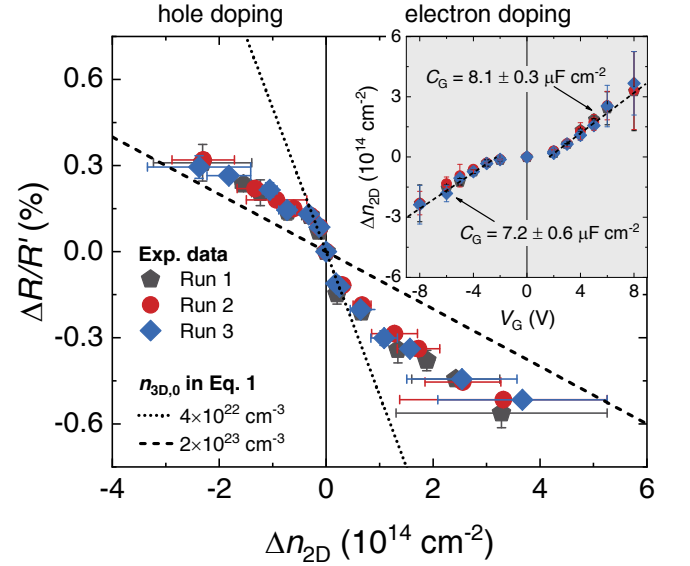


FIG. 3. Normalized resistance variation, $\Delta R/R' = [R_s(\Delta n_{2D}) - R_s(0)]/R_s(\Delta n_{2D})$ as a function of the induced charge density Δn_{2D} obtained upon the step-like application of V_G . Inset: Δn_{2D} as a function of the applied gate voltage V_G determined via double-step chronocoulometry in the same measurements. Dashed lines are linear fits to the data and allow to estimate the gate capacitance C_G .

in our encapsulated NbN films by determining the surface density of induced charge, Δn_{2D} , as a function of V_G . This can be done by means of double-step chronocoulometry, a well-established electrochemical technique [79] which allows determining the charge density stored in the EDL during the FET charging process [1, 2, 9, 10, 21, 30, 32] through the analysis of the I_G transients upon the step-like application and removal of a given value of V_G . As we show in the inset to Fig. 3, the V_G -dependence of Δn_{2D} further demonstrates that gate modulation occurs via charge doping: Δn_{2D} linearly increases upon increasing V_G for both electron and hole doping, as expected for the electrostatic charging of a capacitor. The corresponding gate capacitances ($C_G = 8.1 \pm 0.3$ and $7.2 \pm 0.6 \mu\text{F cm}^{-2}$ as estimated from the linear fits in the electron and hole doping regimes respectively) are also in agreement with a simple estimation of the electrostatic capacitance of a Nb_2O_5 layer with permittivity $\epsilon_r \sim 30$ [80] and thickness $d_{\text{ox}} \simeq 3$ nm, $C_{\text{ox}} = \epsilon_r \epsilon_0 / d_{\text{ox}} \simeq 8.8 \mu\text{F cm}^{-2}$.

Let us now consider the normalized resistance modulation $\Delta R/R' = [R_s(\Delta n_{2D}) - R_s(0)]/R_s(\Delta n_{2D})$ as a function of the induced charge density Δn_{2D} (Fig. 3). This quantity clearly follows two distinct linear trends (highlighted by the straight dashed and dotted lines) in the low- and high- Δn_{2D} regimes. For the sake of comparison, in gated homogeneous films of elemental metals (Au, Ag, Cu) [1, 2], $\Delta R/R'$ displays a simple linear trend, with the same slope in the whole range of Δn_{2D} , that can be described by a simple free-electron model with constant effective mass and relaxation time [1, 2, 21]. The model

predicts that $\Delta R/R'$ should depend on Δn_{2D} according to the equation:

$$\frac{\Delta R}{R'} = \frac{R_s(\Delta n_{2D}) - R_s(0)}{R_s(\Delta n_{2D})} = -\frac{\Delta n_{2D}}{n_{3D,0}t} \quad (1)$$

where $n_{3D,0}$ is the intrinsic carrier density per unit volume and t is the film thickness. Deviations from this trend, with a reduction of the slope, were observed at high gate voltages in ultrathin metallic films ($t \simeq 5$ nm) [1, 2] and were ascribed to scattering phenomena at the film surface, which are not accounted for by Eq. 1 but play a role when the thickness becomes comparable to the mean free path, as well predicted by quantum perturbative scattering models.

In our NbN films, the departure of the data from the initial linear trend cannot be interpreted in the same way, since: i) the mean free path of NbN is known to be very small (approximately 1/10 of the film thickness) so that these films are actually bulk-like [81]; ii) if one uses the thickness of the films $t = 5$ nm, it turns out that the intrinsic carrier density of NbN $n_{3D,0} \simeq 2 \times 10^{23} \text{ cm}^{-3}$ [82] would be compatible with the *high-doping* slope $\Delta R/R'$ (see dashed line in Fig. 3) rather than with the low-doping one, which would instead correspond to $n_{3D,0} \simeq 4 \times 10^{22} \text{ cm}^{-3}$ (dotted line). This indicates that, in the low- V_G regime, the resistance modulation mainly stems from the charge doping of a layer which is less conducting than NbN. This conclusion is supported by the compositional analysis of the films (see X-ray photoelectron spectroscopy analyses below) which evidences the existence of an intermediate interfacial layer of the sub-oxide species $\text{NbO}_x\text{N}_{1-x}$ between the NbN film and the Nb_2O_5 oxide layer. At low gate voltages, this layer is less conductive and less capacitive than NbN [82, 83], absorbs most of the voltage drop through the device and is thus preferentially charge-doped. Eventually, on increasing the gate voltage, its charge density may become similar to that of NbN and the charge induction into the whole NbN film dominates. A more detailed analysis of the $\Delta R/R'$ trend, that takes into account the existence of *two* layers of different materials, is reported in the Supplemental Section V [77].

Incidentally, Fig. 3 also shows that the Nb_2O_5 encapsulation allows safely operating the EDL-FET beyond the electrochemical stability window of the ionic liquid ($|V_G| \leq 6$ V at $T \sim 220$ K): All the resistance modulations induced at $V_G = \pm 8$ V (that correspond to $|\Delta n_{2D}| \gtrsim 2 \times 10^{14} \text{ cm}^{-2}$, see the inset) extrapolate nicely to the linear scaling observed at lower doping levels and the relevant resistance modulations remain reversible – even though a large uncertainty is introduced in the determination of Δn_{2D} due to the large increase in I_G caused by the decomposition of the ionic liquid.

We now consider how the ionic gate modulates the SC properties of our encapsulated NbN ultrathin films, focusing on the dependence of the SC transition temperature T_c on Δn_{2D} . Since the gate-induced T_c shifts can be as small as few millikelvin, we adopt a differential technique

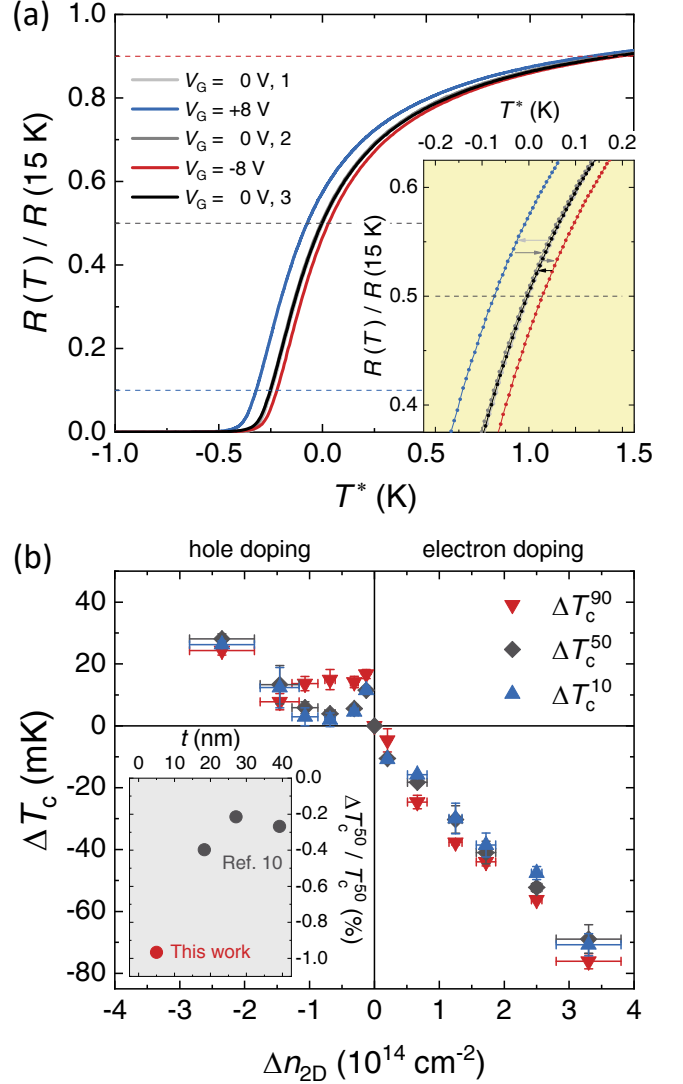


FIG. 4. (a) Normalized resistance $R_s/R_s(15\text{K})$ as a function of the referenced temperature $T^* = [T - T_c^{\text{ref}}]_{V_G} - [T_c^{\text{act}} - T_c^{\text{ref}}]_0$ for different values of the applied gate voltage V_G . Dashed lines highlight the criteria used to obtain T_c^{10} , T_c^{50} , and T_c^{90} from the resistive transitions. Inset: zoom of the same data close to the midpoint of the transition (T_c^{50}). (b) T_c shift ΔT_c as a function of the induced charge density Δn_{2D} determined for T_c^{10} (blue up triangles), T_c^{50} (black diamonds), and T_c^{90} (red down triangles). Inset: maximum T_c tunability $\Delta T_c^{50}/T_c^{50}$ as a function of the NbN film thickness. Black dots are calculated from the data of Ref. 10. The red dot is the maximum tunability achieved in this work.

allowed by the simultaneous measurements of the resistive transition in the active (T_c^{act}) and reference (T_c^{ref}) channels [9, 10, 21]: For each threshold $\tau=10, 50, 90$ (i.e. 10%, 50% and 90% of the resistive transition: see Fig. 4a) the T_c shift due to the application of a certain value of V_G is determined as:

$$\Delta T_c^\tau(V_G) = [T_c^{\tau,\text{act}} - T_c^{\tau,\text{ref}}]_{V_G} - [T_c^{\tau,\text{act}} - T_c^{\tau,\text{ref}}]_0. \quad (2)$$

We will also define a relative temperature scale T^* whose zero falls on the midpoint (50%) of the transition in the reference channel. As a matter of fact, resistance vs. temperature curves at different values of V_G are necessarily recorded in different runs, since the gate voltage can be changed only at high temperature (> 200 K), i.e. above the freezing point of the ionic liquid. Therefore, even the R vs. T curves of the ungated channel may not fall exactly on top of one another, due to a small thermal hysteresis. This does not affect in any way the determination of the T_c shift due to charge accumulation, but may generate confusion when R vs. T curves measured at different V_G are plotted in the same graph. To avoid this problem and improve the readability of the graphs, we will use T^* , defined as: [9, 10, 21]

$$T^* = [T - T_c^{50,\text{ref}}]_{V_G} - [T_c^{50,\text{act}} - T_c^{50,\text{ref}}]_0. \quad (3)$$

The application of positive values of V_G (electron doping) shifts the resistive transition to lower temperatures, while that of negative values of V_G (hole doping) shifts it to higher temperatures (Fig. 4a), consistently with what was reported on thick NbN films [7, 9, 10]. Similarly to the R_s modulations, also the shifts in the resistive transition are fully reversible by simply removing the applied V_G , as shown in the inset to Fig. 4a). This reversible behavior must be compared with the control measurements performed on ultrathin non-encapsulated films, where the T_c suppression upon electron doping was only partially reversible (Fig. S4a), and – most importantly – hole doping not only did not increase T_c but suppressed it in a *completely irreversible* fashion (Fig. S4b) [77]. Notably, the Nb_2O_5 encapsulation allows for this fully reversible behavior to be maintained even for values of V_G in excess of the electrochemical stability window of the ionic liquid (at least up to $V_G = \pm 8$ V), while in non-encapsulated films much smaller values of V_G were sufficient to trigger irreversible modifications – again, consistent with how irreversible T_c shifts were induced in non-encapsulated NbN films when their thickness was reduced below ~ 10 nm in our earlier report [10].

In Fig. 4b we summarize all the T_c shifts measured as a function of Δn_{2D} in our encapsulated films. In the *electron doping* regime, T_c is monotonically suppressed in a nearly linear fashion on increasing Δn_{2D} . Moreover, the T_c shifts are nearly independent of the criterion used to define T_c , i.e. on the threshold τ , which indicates that the resistive transition is rigidly shifted by the charge doping without any appreciable broadening. This is an expected feature for a gated SC film with a thickness smaller than the coherence length [7, 10, 84, 85], since proximity effect “spreads” the perturbation to the SC order parameter well beyond its electrostatic screening length [7, 10, 86] and potentially up to the London penetration depth [65].

In the *hole doping* regime, things are more complicated. The T_c enhancement is found to be almost independent of τ only at large $\Delta n_{2D} \lesssim -2 \times 10^{14} \text{ cm}^{-2}$. At smaller hole doping, ΔT_c^{90} turns out to be nearly doping-independent, but ΔT_c^{50} and ΔT_c^{10} vary in a non-monotonic fashion

Species	Pristine (atom %)	Gated +6 V (atom %)	Gated -6 V (atom %)
NbN	24.2 ± 0.7	22.6 ± 0.7	22.4 ± 0.4
Nb_2O_5	74.6 ± 0.7	74.6 ± 0.6	74.9 ± 0.6
$\text{NbO}_x\text{N}_{1-x}$	1.0 ± 0.2	2.8 ± 0.4	2.7 ± 0.6

TABLE I. XPS peak ratios of the Nb3d region in a pristine NbN film, a NbN film gated at $V_G = +6$ V, and a NbN film gated at $V_G = -6$ V.

as a function of Δn_{2D} and, although always positive, are smaller than ΔT_c^{90} . This indicates a broadening of the SC transition which is instead typically observed in films where the SC order parameter is perturbed in a non-homogeneous way [21, 65]. Overall, this asymmetric tuning of T_c was already observed in thicker, non-encapsulated NbN films [9, 10] and can be ascribed to the similarly asymmetric energy-dependence of the density of states above and below the undoped Fermi level.

Another figure of merit of our encapsulated ultrathin films is the maximum T_c tunability, defined as the maximum value of $|\Delta T_c^{50}|/T_c^{50}$ observed in a given film. If compared to previous results obtained in thicker NbN films [10], the maximum tunability achieved in these ultrathin films is nearly three times larger and approaches 1% (see the inset to Fig. 4b). Notably, this strongly improved tunability is obtained at much lower values of charge doping: $\Delta T_c^{50} \approx -70$ mK is obtained at $\Delta n_{2D} \simeq 3 \times 10^{14} \text{ cm}^{-2}$ in ultrathin encapsulated films, whereas the same T_c shift required attaining $\Delta n_{2D} > 1 \times 10^{15} \text{ cm}^{-2}$ in ~ 10 nm-thick non-encapsulated films in Ref. 10. Further large improvements can be expected by properly optimizing the growth process of the Nb_2O_5 encapsulation layer and increasing its relative permittivity up to $\epsilon_r \sim 90$ [80].

IV. SPECTROSCOPIC CHARACTERIZATION OF THE GATE INTERFACE

As a further support of the effectiveness of the Nb_2O_5 encapsulation layer in ensuring an electrostatic operation of the gated NbN devices, we carried out detailed analyses by means of X-ray photoelectron spectroscopy (XPS). Following a similar protocol as in our previous work [21], three unpatterned films were covered by DEME-TFSI ionic liquid and loaded in the cryocooler with the same procedure as the patterned devices. The first film was not electrically contacted and served as the pristine reference. The other two films were electrically contacted and subjected to $V_G = +6$ V and -6 V at $T = 220$ K, respectively, for ~ 30 min. All the films were then cooled down to the base temperature and warmed up, after which V_G was released in the gated films. All films were then cleaned by subsequent sonications in soapy water, acetone and ethanol (~ 30 min each; the procedure is safe against

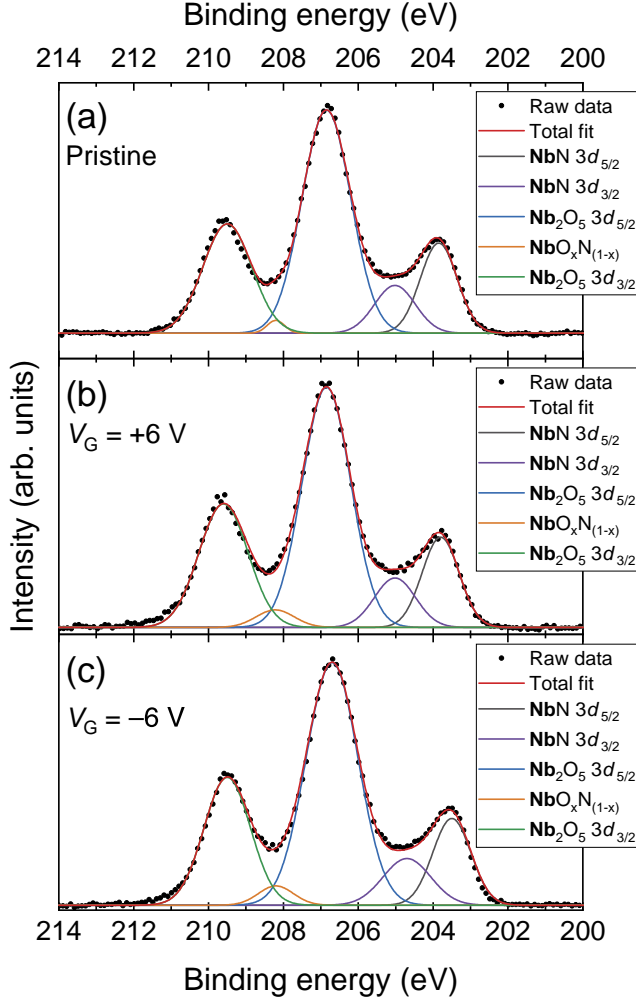


FIG. 5. High-resolution X-ray photoelectron spectroscopy spectra of the Nb3d region in an ungated NbN film (a), a NbN film gated at $V_G = +6$ V (b), and a NbN film gated at $V_G = -6$ V (c). Filled circles are the experimental data, solid lines are the fitted signals and relative components.

modifications of the physical and chemical state of the inorganic components [87, 88]) and blow-dried with a nitrogen gun, after which they were immediately transferred to the ultra-high vacuum chamber of a PHI 5000 Versaprobe scanning X-ray photoelectron spectrometer. XPS spectra were acquired using a monochromatic Al K-alpha X-ray source with 1486.6 eV energy, 15 kV voltage, and 1 mA anode current. Despite the cleaning process, the survey spectra of all samples (Fig. S6 [77]) showed a massive presence of carbon contamination, which is unavoidable since ultra-thin samples cannot be subjected to in-situ Ar-ion milling before the acquisition of the XPS spectra [21]. Such presence of organic species with unknown stoichiometry makes an unambiguous peak assignment of the N and O signals impossible, making their analysis highly speculative at best. We therefore focus on the high-resolution Nb3d spectra shown in Fig. 5, which are unaffected by im-

purities and ionic-liquid residues, and highly sensitive to the chemical environment in both the Nb₂O₅ encapsulation layer and the underlying NbN film. The spectrum of the pristine sample (Fig. 5a) comprises two peaks belonging to NbN ($3d_{5/2}$, ~ 203.8 eV; $3d_{3/2}$, ~ 205.1 eV) [89, 90], two peaks due to the massive presence of Nb₂O₅ ($3d_{5/2}$, ~ 206.9 eV; $3d_{3/2}$, ~ 209.5 eV) [89, 90], and a fifth peak centered at ~ 208.2 eV which can be reasonably assigned to the intermediate suboxide species NbO_xN_{1-x} [91]. This suggests that, even in the pristine sample, the Nb₂O₅ and NbN layers are not separated by a sharp interface but, rather, by an intermediate transition region formed by sub-stoichiometric niobium oxynitride. The spectra of both the gated samples (Fig. 5b, $V_G = +6$ V; Fig. 5c, $V_G = -6$ V) do not show any appreciable difference with respect to the pristine sample in the Nb₂O₅ peaks, as evidenced by the peak areas reported in Table I. Minute differences $\lesssim 2\%$ are instead observed in the NbN peaks and in the NbO_xN_{1-x} peak, which are however extremely sensitive to both fitting procedure and baseline correction. Overall, the XPS analysis indicates that the thickness of the oxynitride transition region might be significantly increased by the gating process, certainly at the expenses of both the NbN film and the Nb₂O₅ encapsulation layer, even though the reduction in the thickness of the latter is, in percentage, very small and experimentally undetectable. Any change to the electronic properties of either the Nb₂O₅ or the NbN layers is instead completely volatile upon removal of the gate voltage.

The increase of the oxynitride transition region and the consequent change in the mean potential barrier of the encapsulation layer is also confirmed by tunnel spectroscopy through the Nb₂O₅ barrier. After a set of ionic gating measurements, we cleaned the surface of the devices and made point contacts (with a conductive Ag paste) on top of either the active (gated) channel or the reference (ungated) channel. A picture of the setup is shown in the inset to Fig. 6a. We then injected a current I into the Ag/Nb₂O₅/NbN junctions and measured the voltage drop $V^+ - V^- = V_{\text{exp}}$ both in the superconductive and in the normal state. This was done in order to determine and cancel the contribution of the spreading resistance r_s (i.e. the portion of NbN film between the point contact and the V^- contact) to the measured $I(V_{\text{exp}})$ curve. Once the measured voltage is suitably corrected [$V(I) = V_{\text{exp}}(I) - r_s I$], we determine the $I(V)$ curve of each junction in the normal state. Fig. 6a reports two examples of such curves, measured on the reference channel (blue symbols) and on the active one (red symbols). Clearly, the latter shows a greater degree of non-linearity that, once the curves are fitted to the simple Simmons' model [92], can be rationalized as being due to a higher thickness and smaller height of the potential barrier that separates the normal electrodes (see Supplemental Section VII for more details [77]). As shown in Fig. 6b and c, this is a general trend; the mean height of the potential barrier is $\langle \phi \rangle_u = 0.60 \pm 0.13$ V before gating, and decreases to $\langle \phi \rangle_g = 0.39 \pm 0.07$ V after gating; at the

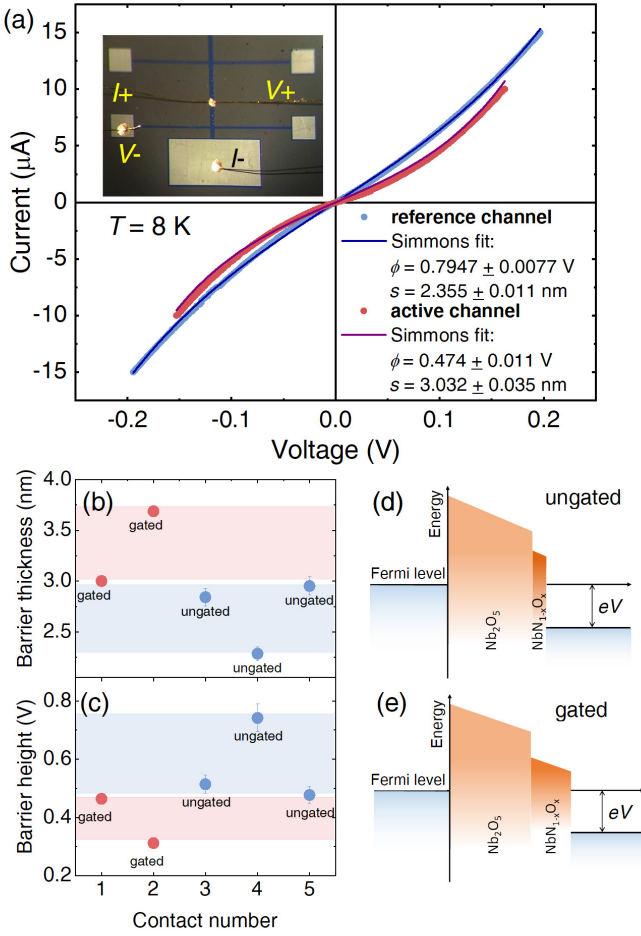


FIG. 6. (a) Two examples of $I(V)$ characteristics of N/I/N junctions made through the Nb oxide layer, in a region of the reference channel (blue symbols) and in a region of the active channel (red symbols). The curves have already been corrected to eliminate the contribution of the spreading resistance. The blue and the red lines represent their fit with the Simmons model [92]. The values of ϕ (barrier height) and s (barrier thickness) extracted from the fit are indicated. For these particular fits, the area of the junctions was fixed to 1.2×10^{-8} m, based on the geometric estimation. The inset shows a picture of the setup. (b) Effective thickness s and (c) effective height ϕ of the potential barrier, as extracted from the Simmons fit of some $I(V)$ curves in the ungated (blue symbols) and gated (red symbols) channels. (d) and (e) summarize in a schematic picture the evolution of the potential barrier upon gating, as it results from XPS and tunnel measurements.

same time, the thickness of the potential barrier increases from $\langle s \rangle_u = 2.62 \pm 0.33$ nm to $\langle s \rangle_g = 3.34 \pm 0.34$ nm. Both these results are compatible with the expansion (by a factor 3: see last line of Table I) of the intermediate interfacial layer of sub-stoichiometric oxide, as observed

via XPS, at the expenses of the NbN film and possibly of the Nb_2O_5 encapsulation layer – provided that one admits, as it seems reasonable, that the relevant potential barrier is lower than that of the insulating oxide. A rough estimation based on the XPS and tunnel data would indicate that the interfacial layer has a thickness of the order of 0.3 nm in the ungated devices, and expands to about 1 nm in the gated ones. A schematic picture of the junction is shown in Figs. 6d and 6e in the ungated and gated devices respectively.

V. CONCLUSIONS

In summary, we have demonstrated a simple and effective method to ensure the volatile and reversible operation of ion-gated superconducting films by means of encapsulation in an ultrathin high- κ dielectric niobium oxide layer. Our gate-dependent electric transport measurements show that encapsulated devices exhibit fully-reversible tunability of both the normal-state resistivity and the superconducting transition temperature, a gate capacitance comparable to that found in non-encapsulated ionic transistors, and stability even beyond the electrochemical stability window of the electrolyte. X-ray photoelectron and tunnel spectroscopy characterizations confirm the effectiveness of the encapsulation layer in suppressing undesired electrochemical interactions between the superconducting film and the electrolyte, and reveal how the only non-volatile alteration to the devices is an increase in the thickness of the substoichiometric interfacial region between the superconducting film and the encapsulation layer. Our approach should be readily transferable to other materials and devices where ensuring a reversible and volatile ionic gate operation without major losses in gate capacitance is required for successful device operation.

ACKNOWLEDGMENTS

We thank S. Guastella and F. Galanti for assistance in the XPS and transport measurements, respectively. We thanks J. Daley and M. K. Mondol of the MIT Nanostructures Laboratory Facility for technical support. We thank E. Batson for assistance in editing the final manuscript. E.P., D.D. and R.S.G. acknowledge funding from the Italian Ministry of Education, University and Research (Project PRIN “Quantum2D”, Grant No. 2017Z8TS5B). M.C., O.M., and K.K.B. acknowledge funding from the National Science Foundation grant ECCS-2000743. M.C. acknowledges support from the Claude E. Shannon Award.

[1] D. Daghero, F. Paolucci, A. Sola, M. Tortello, G. A. Ummarino, M. Agosto, R. S. Gonnelli, J. R. Nair, and

C. Gerbaldi, Large conductance modulation of gold thin

- films by huge charge injection via electrochemical gating, *Phys. Rev. Lett.* **108**, 066807 (2012).
- [2] M. Tortello, A. Sola, K. Sharda, F. Paolucci, J. R. Nair, C. Gerbaldi, D. Daghero, and R. S. Gonnelli, Huge field-effect surface charge injection and conductance modulation in metallic thin films by electrochemical gating, *Appl. Surf. Sci.* **269**, 17 (2013).
 - [3] S. Shimizu, K. S. Takahashi, T. Hatano, M. Kawasaki, Y. Tokura, and Y. Iwasa, Electrically tunable anomalous Hall effect in Pt thin films, *Phys. Rev. Lett.* **111**, 216803 (2013).
 - [4] S. Dushenko, M. Hokazono, K. Nakamura, Y. Ando, T. Shinjo, and M. Shiraishi, Tunable inverse spin Hall effect in nanometer-thick platinum films by ionic gating, *Nat. Commun.* **9**, 3118 (2018).
 - [5] L. Liang, Q. Chen, J. Lu, W. Talsma, J. Shan, G. R. Blake, T. T. Palstra, and J. Ye, Inducing ferromagnetism and kondo effect in platinum by paramagnetic ionic gating, *Sci. Adv.* **4**, eaar2030 (2018).
 - [6] L. Liang, J. Shan, Q. Chen, J. Lu, G. R. Blake, T. T. Palstra, G. E. Bauer, B. Van Wees, and J. Ye, Gate-controlled magnetoresistance of a paramagnetic-insulator—platinum interface, *Phys. Rev. B* **98**, 134402 (2018).
 - [7] E. Piatti, Ionic gating in metallic superconductors: A brief review, *Nano Ex.* **2**, 024003 (2021).
 - [8] J. Choi, R. Pradheesh, H. Kim, H. Im, Y. Chong, and D.-H. Chae, Electrical modulation of superconducting critical temperature in liquid-gated thin niobium films, *Appl. Phys. Lett.* **105**, 012601 (2014).
 - [9] E. Piatti, A. Sola, D. Daghero, G. A. Ummarino, F. Laviano, J. R. Nair, C. Gerbaldi, R. Cristiano, A. Casaburi, and R. S. Gonnelli, Superconducting transition temperature modulation in NbN via EDL gating, *J. Supercond. Novel Magn.* **29**, 587 (2016).
 - [10] E. Piatti, D. Daghero, G. A. Ummarino, F. Laviano, J. R. Nair, R. Cristiano, A. Casaburi, C. Portesi, A. Sola, and R. S. Gonnelli, Control of bulk superconductivity in a BCS superconductor by surface charge doping via electrochemical gating, *Phys. Rev. B* **95**, 140501(R) (2017).
 - [11] F. Paolucci, F. Crisá, G. De Simoni, L. Bours, C. Puglia, E. Strambini, S. Roddaro, and F. Giazotto, Electrostatic field-driven supercurrent suppression in ionic-gated metallic superconducting nanotransistors, *Nano Lett.* **21**, 10309 (2021).
 - [12] M. Yoshida, J. Ye, T. Nishizaki, N. Kobayashi, and Y. Iwasa, Electrostatic and electrochemical tuning of superconductivity in two-dimensional NbSe₂ crystals, *Appl. Phys. Lett.* **108**, 202602 (2016).
 - [13] L. J. Li, E. C. T. O'Farrell, K. P. Loh, G. Eda, B. Özyilmaz, and A. H. Castro Neto, Controlling many-body states by the electric-field effect in a two-dimensional material, *Nature* **529**, 185 (2016).
 - [14] X. Xi, H. Berger, L. Forró, J. Shan, and K. F. Mak, Gate tuning of electronic phase transitions in two-dimensional NbSe₂, *Phys. Rev. Lett.* **117**, 106801 (2016).
 - [15] C. Zhu, J. Cui, B. Lei, N. Wang, C. Shang, F. Meng, L. Ma, X. Luo, T. Wu, Z. Sun, *et al.*, Tuning electronic properties of FeSe_{0.5}Te_{0.5} thin flakes using a solid ion conductor field-effect transistor, *Phys. Rev. B* **95**, 174513 (2017).
 - [16] J. Shiogai, Y. Ito, T. Mitsuhashi, T. Nojima, and A. Tsukazaki, Electric-field-induced superconductivity in electrochemically etched ultrathin FeSe films on SrTiO₃ and MgO, *Nat. Phys.* **12**, 42 (2016).
 - [17] B. Lei, J. Cui, Z. Xiang, C. Shang, N. Wang, G. Ye, X. Luo, T. Wu, Z. Sun, and X. Chen, Evolution of high-temperature superconductivity from a low-T_c phase tuned by carrier concentration in FeSe thin flakes, *Phys. Rev. Lett.* **116**, 077002 (2016).
 - [18] K. Hanzawa, H. Sato, H. Hiramatsu, T. Kamiya, and H. Hosono, Electric field-induced superconducting transition of insulating FeSe thin film at 35 K, *Proc. Natl. Acad. Sci. USA* **113**, 3986 (2016).
 - [19] T. Miyakawa, J. Shiogai, S. Shimizu, M. Matsumoto, Y. Ito, T. Harada, K. Fujiwara, T. Nojima, Y. Itoh, T. Aida, *et al.*, Enhancement of superconducting transition temperature in FeSe electric-double-layer transistor with multivalent ionic liquids, *Phys. Rev. Materials* **2**, 031801(R) (2018).
 - [20] S. Kouno, Y. Sato, Y. Katayama, A. Ichinose, D. Asami, F. Nabeshima, Y. Imai, A. Maeda, and K. Ueno, Superconductivity at 38 K at an electrochemical interface between an ionic liquid and FeSe_{0.8}Te_{0.2} on various substrates, *Sci. Rep.* **8**, 14731 (2018).
 - [21] E. Piatti, T. Hatano, D. Daghero, F. Galanti, C. Gerbaldi, S. Guastella, C. Portesi, I. Nakamura, R. Fujimoto, K. Iida, *et al.*, Ambipolar suppression of superconductivity by ionic gating in optimally doped BaFe₂(As,P)₂ ultrathin films, *Phys. Rev. Materials* **3**, 044801 (2019).
 - [22] K. Ueno, H. Shimotani, H. Yuan, J. Ye, M. Kawasaki, and Y. Iwasa, Field-induced superconductivity in electric double layer transistors, *J. Phys. Soc. Jpn.* **83**, 032001 (2014).
 - [23] T. Fujimoto and K. Awaga, Electric-double-layer field-effect transistors with ionic liquids, *Phys. Chem. Chem. Phys.* **15**, 8983 (2013).
 - [24] P. Gallagher, M. Lee, T. A. Petach, S. W. Stanwyck, J. R. Williams, K. Watanabe, T. Taniguchi, and D. Goldhaber-Gordon, A high-mobility electronic system at an electrolyte-gated oxide surface, *Nat. Commun.* **6**, 6437 (2015).
 - [25] E. Piatti, S. Galasso, M. Tortello, J. R. Nair, C. Gerbaldi, M. Bruna, S. Borini, D. Daghero, and R. S. Gonnelli, Carrier mobility and scattering lifetime in electric double-layer gated few-layer graphene, *Appl. Surf. Sci.* **395**, 37 (2017).
 - [26] Y. Saito and Y. Iwasa, Ambipolar insulator-to-metal transition in black phosphorus by ionic-liquid gating, *ACS Nano* **9**, 3192 (2015).
 - [27] R. S. Gonnelli, E. Piatti, A. Sola, M. Tortello, F. Dolcini, S. Galasso, J. R. Nair, C. Gerbaldi, E. Cappelluti, M. Bruna, *et al.*, Weak localization in electric-double-layer gated few-layer graphene, *2D Mater.* **4**, 035006 (2017).
 - [28] E. Piatti, D. De Fazio, D. Daghero, S. R. Tamalampudi, D. Yoon, A. C. Ferrari, and R. S. Gonnelli, Multi-valley superconductivity in ion-gated MoS₂ layers, *Nano Lett.* **18**, 4821 (2018).
 - [29] D. Ovchinnikov, F. Gargiulo, A. Allain, D. J. Pasquier, D. Dumcenco, C.-H. Ho, O. V. Yazyev, and A. Kis, Disorder engineering and conductivity dome in ReS₂ with electrolyte gating, *Nat. Commun.* **7**, 12391 (2016).
 - [30] E. Piatti, F. Galanti, G. Pippione, A. Pasquarelli, and R. S. Gonnelli, Towards the insulator-to-metal transition at the surface of ion-gated nanocrystalline diamond films, *Eur. Phys. J. Spec. Top.* **228**, 689 (2019).
 - [31] J. Lu, O. Zheliuk, Q. Chen, I. Leermakers, N. E. Hussey, U. Zeitler, and J. Ye, Full superconducting dome of strong

- using protection in gated monolayer WS₂, *Proc. Natl. Acad. Sci. USA* **115**, 3551 (2017).
- [32] E. Piatti, A. Pasquarelli, and R. S. Gonnelli, Orientation-dependent electric transport and band filling in hole co-doped epitaxial diamond films, *Appl. Surf. Sci.* **528**, 146795 (2020).
- [33] S. Zhang, M.-R. Gao, H.-Y. Fu, X.-M. Wang, Z.-A. Ren, and G.-F. Chen, Electric field induced permanent superconductivity in layered metal nitride chlorides HfNCl and ZrNCl, *Chin. Phys. Lett.* **35**, 097401 (2018).
- [34] X. Wang, S. Zhang, H. Fu, M. Gao, Z. Ren, and G. Chen, Dominant role of processing temperature in electric field induced superconductivity in layered ZrNBr, *New J. Phys.* **21**, 023002 (2019).
- [35] D. Zakhidov, D. A. Rehn, E. J. Reed, and A. Salleo, Reversible electrochemical phase change in monolayer to bulk-like MoTe₂ by ionic liquid gating, *ACS Nano* **14**, 2894 (2020).
- [36] Y. Yu, F. Yang, X. F. Lu, Y. J. Yan, Y.-H. Cho, L. Ma, X. Niu, S. Kim, Y.-W. Son, D. Feng, *et al.*, Gate-tunable phase transitions in thin flakes of 1T-TaS₂, *Nat. Nanotechnol.* **10**, 270 (2015).
- [37] W. Shi, J. Ye, Y. Zhang, R. Suzuki, M. Yoshida, J. Miyazaki, N. Inoue, Y. Saito, and Y. Iwasa, Superconductivity series in transition metal dichalcogenides by ionic gating, *Sci. Rep.* **5**, 12534 (2015).
- [38] E. Piatti, Q. Chen, and J. Ye, Strong dopant dependence of electric transport in ion-gated MoS₂, *Appl. Phys. Lett.* **111**, 013106 (2017).
- [39] E. Piatti, Q. Chen, M. Tortello, J. Ye, and R. S. Gonnelli, Possible charge-density-wave signatures in the anomalous resistivity of li-intercalated multilayer MoS₂, *Appl. Surf. Sci.* **461**, 269 (2018).
- [40] B. Lei, Z. Xiang, X. Lu, N. Wang, J. Chang, C. Shang, A. Zhang, Q. Zhang, X. Luo, T. Wu, *et al.*, Gate-tuned superconductor-insulator transition in (Li,Fe)OHFeSe, *Phys. Rev. B* **93**, 060501(R) (2016).
- [41] B. Lei, N. Wang, C. Shang, F. Meng, L. Ma, X. Luo, T. Wu, Z. Sun, Y. Wang, Z. Jiang, *et al.*, Tuning phase transitions in fese thin flakes by field-effect transistor with solid ion conductor as the gate dielectric, *Phys. Rev. B* **95**, 020503(R) (2017).
- [42] Y. Wu, H. Lian, J. He, J. Liu, S. Wang, H. Xing, Z. Mao, and Y. Liu, Lithium ion intercalation in thin crystals of hexagonal TaSe₂ gated by a polymer electrolyte, *Appl. Phys. Lett.* **112**, 023502 (2018).
- [43] D. Kwabena Bediako, M. Rezaee, H. Yoo, D. T. Larson, S. F. Zhao, T. Taniguchi, K. Watanabe, T. L. Brower-Thomas, E. Kaxiras, and P. Kim, Heterointerface effects in the electrointercalation of van der Waals heterostructures, *Nature* **558**, 425 (2018).
- [44] X. Che, Y. Deng, Y. Fang, J. Pan, Y. Yu, and F. Huang, Gate-tunable electrical transport in thin 2M-WS₂ flakes, *Adv. Electron. Mater.* **5**, 1900462 (2019).
- [45] C. Shang, B. Lei, W. Zhuo, Q. Zhang, C. Zhu, J. Cui, X. Luo, N. Wang, F. Meng, L. Ma, *et al.*, Structural and electronic phase transitions driven by electric field in metastable MoS₂ thin flakes, *Phys. Rev. B* **100**, 020508(R) (2019).
- [46] Y. Song, X. Liang, J. Guo, J. Deng, G. Gao, and X. Chen, Superconductivity in Li-intercalated 1T-SnSe₂ driven by electric field gating, *Phys. Rev. Materials* **3**, 054804 (2019).
- [47] N. Lu, P. Zhang, Q. Zhang, R. Qiao, Q. He, H.-B. Li, Y. Wang, J. Guo, D. Zhang, Z. Duan, *et al.*, Electric-field control of tri-state phase transformation with a selective dual-ion switch, *Nature* **546**, 124 (2017).
- [48] X. Leng, J. Pereiro, J. Strle, G. Dubuis, A. Bollinger, A. Gozar, J. Wu, N. Litombe, C. Panagopoulos, D. Pavuna, *et al.*, Insulator to metal transition in WO₃ induced by electrolyte gating, *npj Quant. Mater.* **2**, 35 (2017).
- [49] Y. Cui, G. Zhang, H. Li, H. Lin, X. Zhu, H.-H. Wen, G. Wang, J. Sun, M. Ma, Y. Li, *et al.*, Protonation induced high-T_c phases in iron-based superconductors evidenced by nmr and magnetization measurements, *Sci. Bull.* **63**, 11 (2018).
- [50] M. Rafique, Z. Feng, Z. Lin, X. Wei, M. Liao, D. Zhang, K. Jin, and Q.-K. Xue, Ionic liquid gating induced protonation of electron-doped cuprate superconductors, *Nano Lett.* **19**, 7775 (2019).
- [51] Y. Cui, Z. Hu, J.-S. Zhang, W.-L. Ma, M.-W. Ma, Z. Ma, C. Wang, J.-Q. Yan, J.-P. Sun, J.-G. Cheng, *et al.*, Ionic-liquid-gating induced protonation and superconductivity in FeSe, FeSe_{0.93}S_{0.07}, ZrNCl, 1T-TaS₂ and Bi₂Se₃, *Chin. Phys. Lett.* **36**, 077401 (2019).
- [52] Z. Li, S. Shen, Z. Tian, K. Hwangbo, M. Wang, Y. Wang, F. M. Bartram, L. He, Y. Lyu, Y. Dong, *et al.*, Reversible manipulation of the magnetic state in SrRuO₃ through electric-field controlled proton evolution, *Nat. Commun.* **11**, 184 (2020).
- [53] Y. Meng, X. Xing, X. Yi, B. Li, N. Zhou, M. Li, Y. Zhang, W. Wei, J. Feng, K. Terashima, *et al.*, Protonation-induced discrete superconducting phases in bulk FeSe single crystals, *Phys. Rev. B* **105**, 134506 (2022).
- [54] E. Piatti, G. Prando, M. Meinero, C. Tresca, M. Putti, S. Roddaro, G. Lamura, T. Shiroka, P. Carretta, G. Profeta, D. Daghero and R. S. Gonnelli. Coexisting superconductivity and charge-density wave in hydrogen-doped titanium diselenide via ionic liquid gating-induced protonation. *arXiv:2205.12951*.
- [55] J. Jeong, N. Aetukuri, T. Graf, T. D. Schladt, M. G. Samant, and S. S. Parkin, Suppression of metal-insulator transition in VO₂ by electric field-induced oxygen vacancy formation, *Science* **339**, 1402 (2013).
- [56] T. D. Schladt, T. Graf, N. B. Aetukuri, M. Li, A. Fantini, X. Jiang, M. G. Samant, and S. S. Parkin, Crystal-facet-dependent metallization in electrolyte-gated rutile tio₂ single crystals, *ACS Nano* **7**, 8074 (2013).
- [57] T. A. Petach, M. Lee, R. C. Davis, A. Mehta, and D. Goldhaber-Gordon, Mechanism for the large conductance modulation in electrolyte-gated thin gold films, *Phys. Rev. B* **90**, 081108(R) (2014).
- [58] S. Maruyama, J. Shin, X. Zhang, R. Suchoski, S. Yasui, K. Jin, R. Greene, and I. Takeuchi, Reversible electrochemical modulation of the superconducting transition temperature of LiTi₂O₄ ultrathin films by ionic liquid gating, *Appl. Phys. Lett.* **107**, 142602 (2015).
- [59] J. Walter, H. Wang, B. Luo, C. D. Frisbie, and C. Leighton, Electrostatic versus electrochemical doping and control of ferromagnetism in ion-gel-gated ultrathin La_{0.5}Sr_{0.5}CoO_{3-δ}, *ACS Nano* **10**, 7799 (2016).
- [60] L. Zhang, S. Zeng, X. Yin, T. C. Asmara, P. Yang, K. Han, Y. Cao, W. Zhou, D. Wan, C. S. Tang, *et al.*, The mechanism of electrolyte gating on high-t_c cuprates: the role of oxygen migration and electrostatics, *ACS Nano* **11**, 9950 (2017).

- [61] S. Zeng, X. Yin, T. Herng, K. Han, Z. Huang, L. Zhang, C. Li, W. Zhou, D. Wan, P. Yang, *et al.*, Oxygen electromigration and energy band reconstruction induced by electrolyte field effect at oxide interfaces, *Phys. Rev. Lett.* **121**, 146802 (2018).
- [62] M. S. Saleem, B. Cui, C. Song, Y. Sun, Y. Gu, R. Zhang, M. U. Fayaz, X. Zhou, P. Werner, S. S. Parkin, *et al.*, Electric field control of phase transition and tunable resistive switching in SrFeO_{2.5}, *ACS Appl. Mater. Interfaces* **11**, 6581 (2019).
- [63] Y. Zhang, T. Oka, R. Suzuki, J. Ye, and Y. Iwasa, Electrically switchable chiral light-emitting transistor, *Science* **344**, 725 (2014).
- [64] Q. Chen, J. Lu, L. Liang, O. Zheliuk, A. Ali El Yumin, and J. Ye, Continuous low-bias switching of superconductivity in a MoS₂ transistor, *Adv. Mater.* **30**, 1800399 (2018).
- [65] G. De Simoni, F. Paolucci, P. Solinas, E. Strambini, and F. Giazotto, Metallic supercurrent field-effect transistor, *Nat. Nanotechnol.* **13**, 802 (2018).
- [66] F. Paolucci, G. De Simoni, E. Strambini, P. Solinas, and F. Giazotto, Ultra-efficient superconducting Dayem bridge field-effect transistor, *Nano Lett.* **18**, 4195 (2018).
- [67] F. Paolucci, G. De Simoni, P. Solinas, E. Strambini, N. Ligato, P. Virtanen, A. Braggio, and F. Giazotto, Magnetotransport experiments on fully metallic superconducting Dayem-bridge field-effect transistors, *Phys. Rev. Applied* **11**, 024061 (2019).
- [68] F. Paolucci, F. Vischi, G. De Simoni, C. Guarcello, P. Solinas, and F. Giazotto, Field-effect controllable metallic Josephson interferometer, *Nano Lett.* **19**, 6263 (2019).
- [69] J. H. Cho, J. Lee, Y. Xia, B. Kim, Y. He, M. J. Renn, T. P. Lodge, and C. D. Frisbie, Printable ion-gel gate dielectrics for low-voltage polymer thin-film transistors on plastic, *Nat. Mater.* **7**, 900 (2008).
- [70] S.-K. Lee, S. H. Kabir, B. K. Sharma, B. J. Kim, J. H. Cho, and J.-H. Ahn, Photo-patternable ion gel-gated graphene transistors and inverters on plastic, *Nanotechnology* **25**, 014002 (2014).
- [71] E. Piatti, A. Arbab, F. Galanti, T. Carey, L. Anzi, D. Spurling, A. Roy, A. Zhussupbekova, K. A. Patel, J. M. Kim, *et al.*, Charge transport mechanisms in inkjet-printed thin-film transistors based on two-dimensional materials, *Nat. Electron.* **4**, 893 (2021).
- [72] S. Shimizu, J. Shiogai, N. Takemori, S. Sakai, H. Ikeda, R. Arita, T. Nojima, A. Tsukazaki, and Y. Iwasa, Giant thermoelectric power factor in ultrathin FeSe superconductor, *Nat. Commun.* **10**, 825 (2019).
- [73] W. Huang, Y. Zhang, M. Song, B. Wang, H. Hou, X. Hu, X. Chen, and T. Zhai, Encapsulation strategies on 2D materials for field effect transistors and photodetectors, *Chinese Chemical Letters*, In press (2021).
- [74] H. Jo, J.-H. Choi, C.-M. Hyun, S.-Y. Seo, C.-M. Kim, M.-J. Lee, J.-D. Kwon, H.-S. Moon, S.-H. Kwon, J.-H. Ahn, *et al.*, A hybrid gate dielectrics of ion gel with ultra-thin passivation layer for high-performance transistors based on two-dimensional semiconductor channels, *Sci. Rep.* **7**, 14194 (2017).
- [75] A. E. Dane, A. N. McCaughan, D. Zhu, Q. Zhao, C.-S. Kim, N. Calandri, A. Agarwal, F. Bellei, and K. K. Berggren, Bias sputtered NbN and superconducting nanowire devices, *Appl. Phys. Lett.* **111**, 122601 (2017).
- [76] O. Medeiros, M. Colangelo, I. Charaev, and K. K. Berggren, Measuring thickness in thin NbN films for superconducting devices, *J. Vac. Sci. Technol. A* **37**, 041501 (2019).
- [77] See the Supplemental Material at [insert link here] for a detailed description of the samples and the fabrication process, the full response of an encapsulated ultrathin film to a triangular gate voltage wave, the sheet resistance modulation at low temperatures, the control experiments in non-encapsulated ultrathin films, the parallel-resistor model for the resistance modulation, and additional details on the X-ray photoelectron spectroscopy of encapsulated ultrathin films and on the measurement and fitting of the tunnelling V(I) curves.
- [78] Y. Zhou and S. Ramanathan, Relaxation dynamics of ionic liquid-VO₂ interfaces and influence in electric double-layer transistors, *J. Appl. Phys.* **111**, 084508 (2012).
- [79] F. Scholtz, *Electroanalytical Methods* (Springer-Verlag, Berlin Heidelberg, 2010).
- [80] A. Pignolet, G. M. Rao, and S. B. Krupanidhi, Rapid thermal processed thin films of niobium pentoxide (Nb₂O₅) deposited by reactive magnetron sputtering, *Thin Solid Films* **261**, 18 (1995).
- [81] K. Fuchs, The conductivity of thin metallic films according to the electron theory of metals, *Mathematical Proceedings of the Cambridge Philosophical Society* **34**, 100 108 (1938).
- [82] S. P. Chockalingam, M. Chand, J. Jesudasan, V. Tripathi, and P. Raychaudhuri, Superconducting properties and Hall effect of epitaxial NbN thin films, *Phys. Rev. B* **77**, 214503 (2008).
- [83] T. S. El-Shazly, W. M. Hassan, S. S. Abd-el Rehim, and N. K. Allam, Optical and electronic properties of niobium oxynitrides with various N/O ratios: insights from first-principles calculations, *J. Photonics Energy* **8**, 026501 (2018).
- [84] G. A. Ummarino, E. Piatti, D. Daghero, R. S. Gonnelli, I. Y. Sklyadneva, E. V. Chulkov, and R. Heid, Proximity Eliashberg theory of electrostatic field-effect doping in superconducting films, *Phys. Rev. B* **96**, 064509 (2017).
- [85] G. A. Ummarino and D. Romanin, Theoretical explanation of electric field-induced superconductive critical temperature shifts in indium thin films, *Phys. Status Solidi B* **257**, 1900651 (2020).
- [86] E. Piatti, D. Romanin, R. S. Gonnelli, and D. Daghero, Anomalous screening of an electrostatic field at the surface of niobium nitride, *Appl. Surf. Sci.* **461**, 17 (2018).
- [87] I. Charaev, T. Silbernagel, B. Bachowsky, A. Kuzmin, S. Doerner, K. Ilin, A. Semenov, D. Roditchev, D. Y. Vodolazov, and M. Siegel, Enhancement of superconductivity in NbN nanowires by negative electron-beam lithography with positive resist, *J. Appl. Phys.* **122**, 083901 (2017).
- [88] M. K. Neylon, S. K. Bej, C. A. Bennett, and L. T. Thompson, Ethanol amination catalysis over early transition metal nitrides, *Appl. Catal. A - Gen.* **232**, 13 (2002).
- [89] A. Ermolieff, M. Girard, C. Raoul, C. Bertrand, and T. M. Duc, An XPS comparative study on thermal oxide barrier formation on Nb and NbN thin films, *Appl. Surf. Sci.* **21**, 65 (1985).
- [90] Z. Lan, H. Fu, R. Zhao, H. Liu, W. Zhou, H. Ning, and J. Guo, Roles of in situ-formed NbN and Nb₂O₅ from N-doped Nb₂C MXene in regulating the re/hydrogenation and cycling performance of magnesium hydride, *Chem. Eng. J.* **431**, 133985 (2022).
- [91] A. Darlinski and J. Halbritter, Angle-resolved XPS studies of oxides at NbN, NbC, and Nb surfaces, *Surf. Interface*

Anal. **10**, 223 (1987).

[92] J. G. Simmons, Generalized formula for the electric tunnel effect between similar electrodes separated by a thin insulating film, *J. Appl. Phys.* **34**, 1793 (1963).

Reversible Tuning of Superconductivity in Ion-Gated NbN Ultrathin Films by Self-Encapsulation with a High- κ Dielectric Layer

Supplemental Material

Erik Piatti,^{1,*} Marco Colangelo,^{2,*} Mattia Bartoli,^{3,4} Owen Medeiros,²
Renato S. Gonnelli,¹ Karl K. Berggren,² and Dario Daghero^{1,†}

¹*Department of Applied Science and Technology, Politecnico di Torino, I-10129 Torino, Italy*

²*Department of Electrical Engineering and Computer Science,
Massachusetts Institute of Technology, Cambridge, MA 02139, USA*

³*Center for Sustainable Future Technologies-CSFT@POLITO, I-10144 Torino, Italy*

⁴*Consorzio Interuniversitario Nazionale per la Scienza e Tecnologia dei Materiali (INSTM), I-850121 Firenze, Italy*

CONTENTS

I. Samples and fabrication process	2
II. Full response of an encapsulated ultrathin film to a triangular gate voltage wave	3
III. Sheet resistance modulation at low temperatures	3
IV. Control experiments in non-encapsulated ultrathin films	4
V. The parallel-resistor model for the resistance modulation	5
VI. X-ray photoelectron spectroscopy of encapsulated ultrathin films	7
VII. Measurement and fitting of the tunnelling $V(I)$ curves	8
References	8

* These authors contributed equally.

† dario.daghero@polito.it

I. SAMPLES AND FABRICATION PROCESS

The Hall bar structure was fabricated starting from a ≈ 5 nm-thick NbN layer deposited on a substrate with a 300 nm-thick thermal oxide layer on silicon. Details on the deposition process (room temperature reactive sputtering) can be found in Ref. [?]. The Hall bar was patterned with a direct writing lithography process. The sample was spin-coated with a 1.2 μ m-thick layer of Microposit S1813 resist. The resist was patterned using Heidelberg μ PG 101. The pattern was developed in Microposit MF-CD-26 and transferred into the NbN with reactive ion etching in CF_4 plasma. Gold pads were fabricated on the Hall bar leads to simplify the electrical contact. The sample was spin-coated with a 500 nm-thick layer of NANO PMGI SF9 and a 1.2 μ m-thick layer of Microposit S1813. The patterns for the pads were defined with aligned direct writing lithography using Heidelberg μ PG 101 and developed in Microposit MF-CD-26. A 5 nm-thick titanium adhesion layer and a 20 nm-thick gold layer were deposited with electron-beam evaporation and lifted off in 1-Methyl-2-pyrrolidinone. To grow the encapsulation layers, the samples were annealed with a rapid thermal annealing (RTA) process. The samples used for electrical characterization and measurements were annealed for a total of 20 minutes at 200 degrees Celsius with 5 SPLM oxygen. The samples used for XPS were annealed for a total of 20 minutes at 200 degrees Celsius with 1 SPLM oxygen. This difference in annealing methods was caused by the dismissal of the first RTA tool during the experiments. In Table I, we show the thickness of NbN and Nb_2O_5 measured with ellipsometry [?] after the annealing process. For the Hall bar sample, the measurement was performed on a monitor chip, with a NbN film nominally identical (from the same deposition batch) to the Hall bar device.

Sample	NbN	Nb_2O_5
Hall bar (monitor sample)	5.73 nm	2.06 nm
XPS	5.21 nm	2.66 nm

TABLE I. Thickness of samples used for the experiments.

II. FULL RESPONSE OF AN ENCAPSULATED ULTRATHIN FILM TO A TRIANGULAR GATE VOLTAGE WAVE

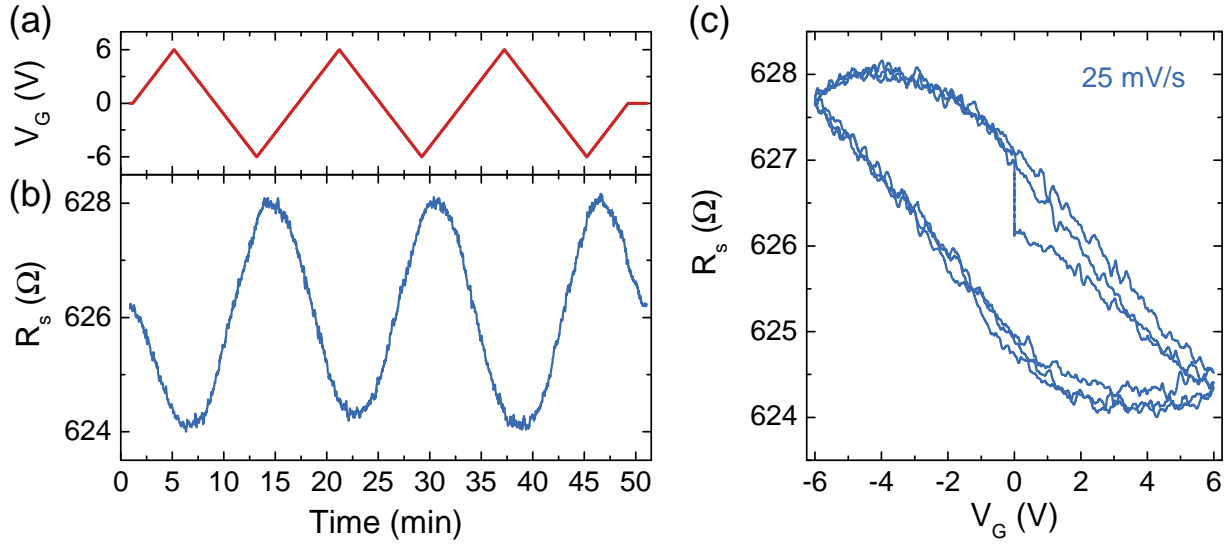


FIG. S1. (a) Application of a triangular gate voltage V_G wave with a sweep rate of 25 mV s^{-1} , and (b) typical response of R_s in an encapsulated NbN film at $T = 220 \text{ K}$. (c) Corresponding R_s vs. V_G curves.

III. SHEET RESISTANCE MODULATION AT LOW TEMPERATURES

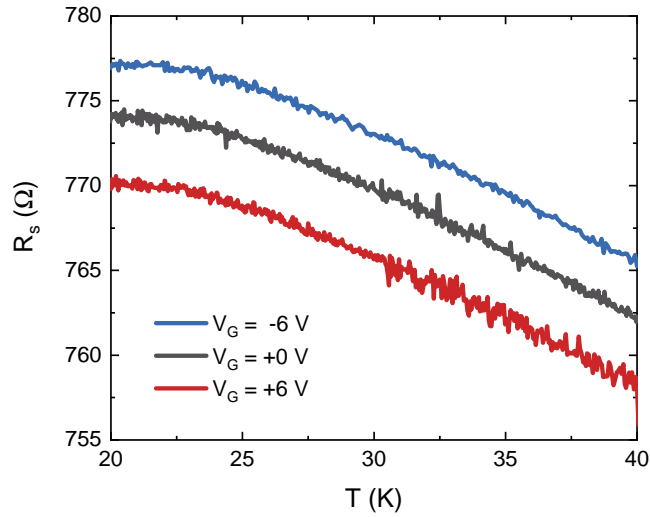


FIG. S2. Sheet resistance R_s of the gated channel as a function of temperature T between 20 and 40 K, for three different values of V_G . The clear gate-induced modulation of R_s can be observed even in this T range way below the freezing point of the ionic liquid, where the gate leakage current is zero due to the complete halt of any ionic motion.

IV. CONTROL EXPERIMENTS IN NON-ENCAPSULATED ULTRATHIN FILMS

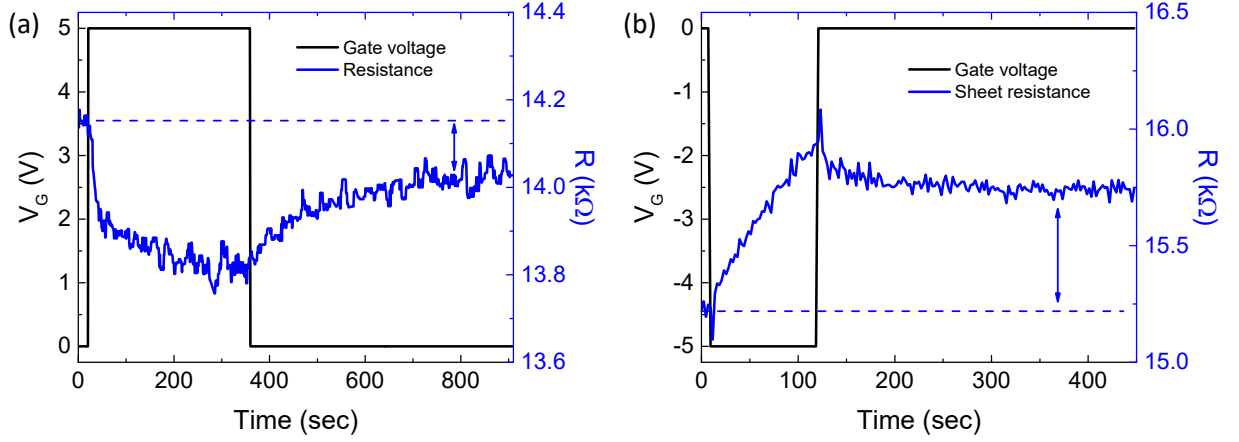


FIG. S3. Typical response of R_s (blue line, right scale) to the step-like application and removal of positive (a) and negative (b) values of V_G (black line, left scale) at $T = 220$ K in a non-encapsulated ultrathin NbN film. The blue arrows indicate the amount of non-reversible R_s modulation upon removal of the applied V_G .

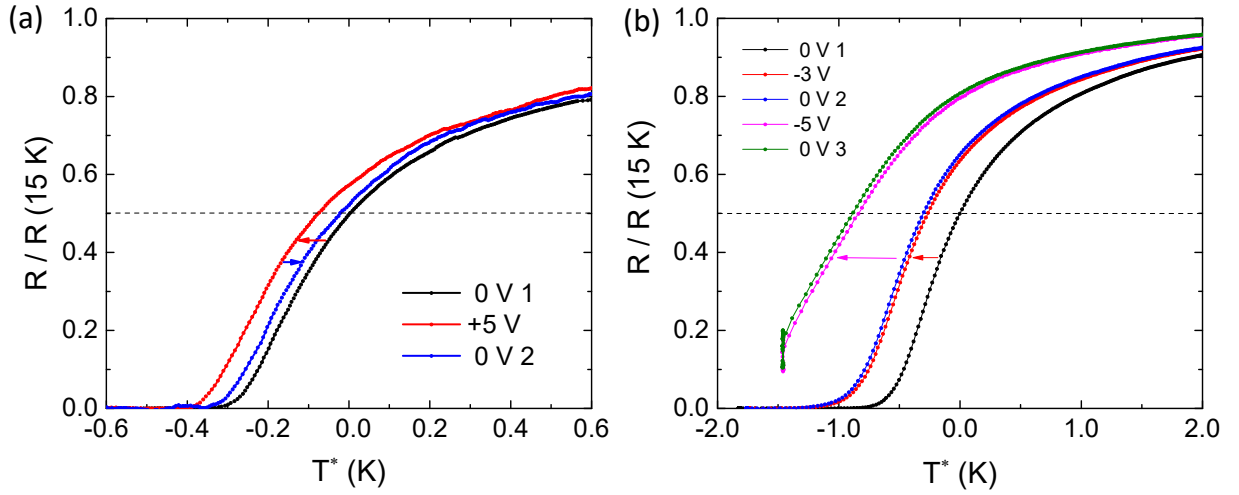


FIG. S4. Normalized resistance $R_s/R_s(15\text{ K})$ vs. referenced temperature $T^* = [T - T_c^{\text{ref}}]_{V_G} - [T_c^{\text{act}} - T_c^{\text{ref}}]_0$ for different values of the applied gate voltage V_G in a non-encapsulated ultrathin NbN film. Dashed lines highlight the criteria used to obtain T_c^{50} from the resistive transitions. Arrows highlight the order in which the measurements were performed.

V. THE PARALLEL-RESISTOR MODEL FOR THE RESISTANCE MODULATION

In order to properly interpret the trend of the normalized resistance modulation $\Delta R/R'$ as a function of Δn_{2D} , we must generalize the free-electron model we used for homogeneous films [?] to account for the presence of the oxynitride layer on top of the NbN film. Let us assume that the film has length ℓ and width w and is made of two layers of thickness d_1 (the oxynitride layer) and d_2 (the underlying NbN layer), respectively. Let n_i , m_i and τ_i be the unperturbed *volume* density of charge carriers, the effective mass and the scattering lifetime of the i -th layer. If z is the axis normal to the interface, the additional charge induced by the electric field clearly follows a density profile $\Delta n_{3D}(z)$, which decays on a length scale defined by the screening length ξ . In materials with high intrinsic carrier density, ξ is usually thought to be of the order of the Thomas-Fermi screening length λ_{TF} . However, as experimentally observed, and as demonstrated by first-principle calculations in the FET configuration [?], in the presence of the very intense fields reached in ionic-gating experiments the linear Thomas-Fermi approximation breaks down and the screening length increases (well beyond λ_{TF}) as a function of the effective surface density of induced charges, Δn_{2D} . Indeed, as shown in Ref.?, everything happens as if there were a saturation in the volume charge density and, consequently, an extension of the depth of the layer of charge accumulation when the total induced charge increases. In the case of NbN, this depth can become as large as a few nanometers for $\Delta n_{2D} > 10^{15} \text{ cm}^{-2}$.

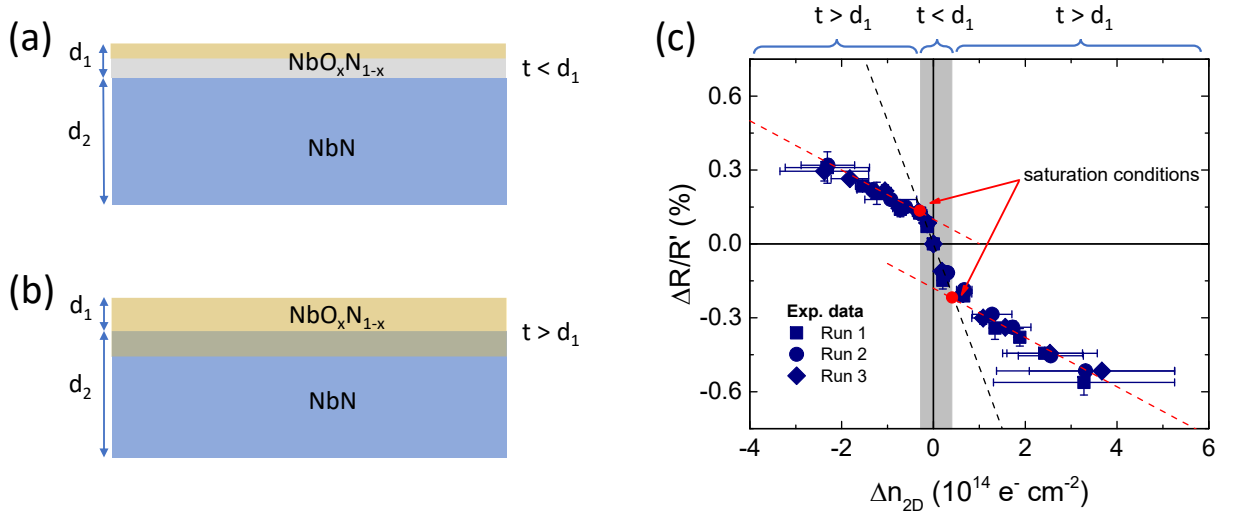


FIG. S5. (a, b) Scheme of the charge accumulation in the NbN films (blue), taking into account the presence of the oxynitride layer (grey). The charge accumulation layer is depicted in yellow. In the low-field regime it is limited to the oxynitride layer (a) while in the high-field regime it extends down to the NbN film (b). The two regimes are separated by the saturation point in which $t = d_1$. (c) Experimental behaviour of $\Delta R/R'$ as a function of Δn_{2D} (blue symbols) together with the linear trends that approximate it in the low-field (black dashed line) and in the high-field (red dashed lines) regime. The red point indicates the saturation point.

Here, as we did in the case of homogeneous films[?] we will choose for $\Delta n_{3D}(z)$ a step profile, thus assuming for simplicity that the induced charge is uniformly distributed within a depth t that acts as an effective screening length. However, the presence of two layers of different materials, with very different intrinsic properties, forces us to consider them separately. In the absence of field (no gate voltage) the conductance of the compound slab is

$$G_0 = \frac{e^2 w}{\ell} \left(\frac{n_1 \tau_1}{m_1} d_1 + \frac{n_2 \tau_2}{m_2} d_2 \right) = \frac{e^2 w}{\ell} (n_1 A_1 d_1 + n_2 A_2 d_2) \quad (1)$$

having defined the parameters

$$A_i = \tau_i / m_i$$

that are material-dependent and account for the bandstructure and the scattering lifetime. When a small gate voltage is applied, induced charges accumulate only in the topmost layer, i.e. $t < d_1$ (see Fig. S5a). Let us call n'_1 the perturbed volume charge density, which is uniform in the accumulation layer, and is such that $\Delta n_{2D} = (n'_1 - n_1)t$. In these conditions, the conductance of the compound slab is:

$$G_1 = \frac{e^2 w}{\ell} [n'_1 A_1 t + n_1 A_1 (d_1 - t) + n_2 A_2 d_2]. \quad (2)$$

The normalized resistance variation is thus

$$\frac{\Delta R}{R'} = \frac{G_0 - G_1}{G_0} = -(n'_1 - n_1)t \frac{A_1}{n_1 A_1 d_1 + n_2 A_2 d_2} = -\Delta n_{2D} \frac{A_1}{n_1 A_1 d_1 + n_2 A_2 d_2}. \quad (3)$$

This equation corresponds to the low-field region of the experimental curves, i.e. it describes the black dashed line in Fig. S5c. On increasing the electric field and the total induced charge, the thickness of the accumulation layer t increases. When it becomes equal to d_1 (that means that the whole oxynitride layer has been perturbed) the normalized resistance variation reaches the saturation value (red point in Fig. S5c):

$$\left. \frac{\Delta R}{R'} \right|_{\text{sat}} = -(n'_1 - n_1)d_1 \frac{A_1}{n_1 A_1 d_1 + n_2 A_2 d_2} = -\Delta n_{2D, \text{sat}} \frac{A_1}{n_1 A_1 d_1 + n_2 A_2 d_2}. \quad (4)$$

On further increasing the field, the contribution of the oxynitride layer to the slab conductance remains constant, but the accumulation layer extends beyond d_1 and the charge induction interests also the underlying NbN layer (Fig. S5b). In the conditions where $t > d_1$, and calling $t' = t - d_1$ the thickness of the NbN layer interested by charge accumulation, one obtains that the conductance of the compound slab is

$$G_2 = \frac{e^2 w}{\ell} [n'_1 A_1 d_1 + n'_2 A_2 t' + n_2 A_2 (d_2 - t')]. \quad (5)$$

and the normalized resistance variation is

$$\frac{\Delta R}{R'} = \frac{G_0 - G_2}{G_0} = -(n'_1 - n_1)d_1 \frac{A_1}{n_1 A_1 d_1 + n_2 A_2 d_2} - (n'_2 - n_2)t' \frac{A_2}{n_1 A_1 d_1 + n_2 A_2 d_2} \quad (6)$$

$$= \left. \frac{\Delta R}{R'} \right|_{\text{sat}} - (\Delta n_{2D} - \Delta n_{2D, \text{sat}}) \frac{A_2}{n_1 A_1 d_1 + n_2 A_2 d_2} \quad (7)$$

$$= -\Delta n_{2D} \frac{A_2}{n_1 A_1 d_1 + n_2 A_2 d_2} + \text{const.} \quad (8)$$

This equation corresponds to the red dashed line in Fig. S5c that approximates the high-field linear behaviour of the experimental points. By comparing Eqs. 3 and 8, it turns out that the slopes of the $\Delta R/R'$ vs Δn_{2D} curves in the two regimes are different because of the different properties of the two materials. Here we have assumed that neither τ_i nor m_i are affected by the charge perturbation, so that the A_i are always equal to their intrinsic values – an approximation which is reasonable for materials with a high intrinsic carrier density. The ratio between the two slopes turns out to be equal to the ratio A_2/A_1 . Experimentally, this ratio is equal to 0.2, which means that $A_1 = 5A_2$. This result is reasonable, at least if the contribution of the effective mass is considered, since niobium oxynitrides are predicted to exhibit smaller effective masses with respect to stoichiometric NbN [? ?].

Up to now, we have not used the experimental information about the thickness of the layers, but only about the slope of the experimental points in Fig. S5. However, starting from Eq. 4 and using the coordinates of the saturation point (for electron doping) $\left. \frac{\Delta R}{R'} \right|_{\text{sat}} = -0.217 \times 10^{-2}$ and $\Delta n_{2D, \text{sat}} = 0.407 \times 10^{14} \text{ cm}^{-2}$, together with the fact that $A_1 = 5A_2$, one can obtain

$$5n_1 d_1 + n_2 d_2 = 9.38 \cdot 10^{16} \text{ cm}^{-2}.$$

Approximating the experimental values of the thicknesses obtained by tunnel spectroscopy, XPS and ellipsometry to $d_1 \simeq 1 \text{ nm}$ and $d_2 \simeq 5 \text{ nm}$, this equation provides

$$n_1 + n_2 \simeq 1.88 \cdot 10^{23} \text{ cm}^{-3}$$

which is of the proper order of magnitude. Although we cannot obtain n_1 and n_2 separately, this result somehow refines the rough estimation of the intrinsic 3D charge density provided in the main text, which was based solely on the slopes of $\Delta R/R'$ as a function of Δn_{2D} and was extracted by using the parallel-resistor model in the case of a *homogeneous* material (thus neglecting the fact that the slab is actually made of two layers). In that case, the slope is simply $-1/n_{3D}d$ and the estimated $n_1 = 2 \times 10^{23} \text{ cm}^{-3}$, $n_2 = 0.4 \times 10^{23} \text{ cm}^{-3}$ were obtained by taking d as the (approximated) total thickness of the slab.

VI. X-RAY PHOTOELECTRON SPECTROSCOPY OF ENCAPSULATED ULTRATHIN FILMS

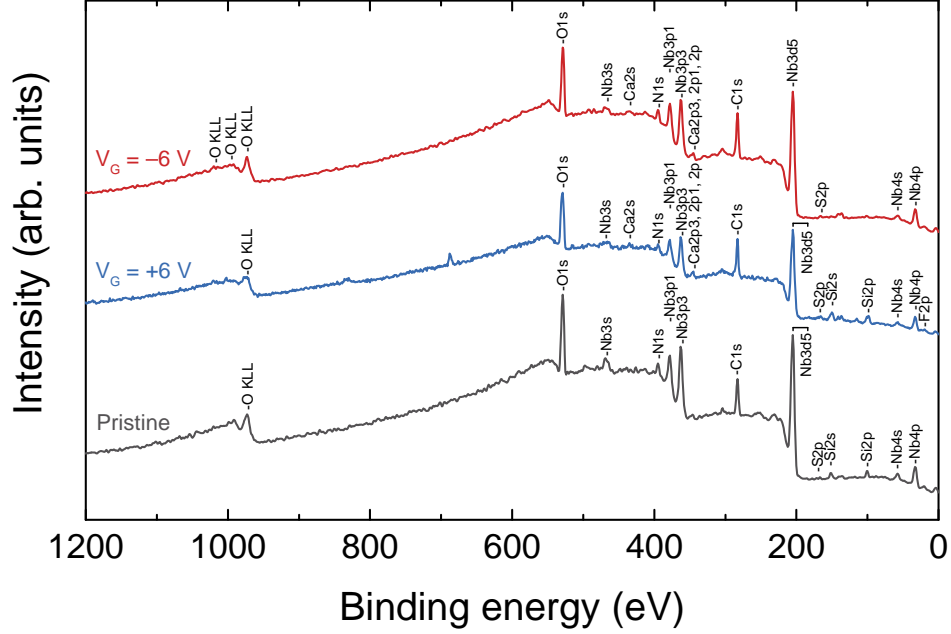


FIG. S6. X-ray photoelectron spectroscopy survey scans of a pristine NbN film (black line), a NbN film gated at $V_G = +6$ V (blue line), and a NbN film gated at $V_G = -6$ V (red line), together with peak assignments obtained using the Multi Pak Software 9.7 for peak recognition.

X-ray photoelectron spectroscopy measurements were performed on three samples cut from the same large-area, unpatterned film: a pristine film, a film gated at $V_G = +6$ V, and a film gated at $V_G = -6$ V, as discussed in the Main Text. The survey spectra of all three samples (shown in Fig. S6) show a massive presence of carbon contamination. Considering that all films were exposed to the DEME-TFSI ionic liquid and were coated by a protective polymethyl methacrylate (PMMA) layer during storage and shipping, it is reasonable to assume that the carbon contamination is due to residues arising from both, which could not be fully removed by the cleaning process prior to the XPS measurements. Within this surface contamination layer, the amount of ionic liquid is reasonably inferior compared with that of PMMA, as suggested by the small sulphur signal as reported in Table II, from the oxygen spectra, and from the ionic liquid composition (DEME-TFSI Elemental Analysis: C 28.17%; H 4.73%; F 26.73%; N 6.57%; O 18.76%; S 15.04%). Different silicon percentages arising from the underlying SiO_2 substrate were detected in the three samples, which were reasonably due to a slightly different thickness of the $\text{Nb}_2\text{O}_5/\text{NbN}$ stack in each analysis spot.

Element	Pristine (atom %)	Gated +6 V (atom %)	Gated -6 V (atom %)
C	34	36	43
O	38	31	33
N	7	6	7
Nb	17	11	15
S	4	2	1
Si	<1	9	1
Ca	Not detected	1	Not detected
F	Not detected	4	Not detected

TABLE II. Atomic compositions of a pristine NbN film, a NbN film gated at $V_G = +6$ V, and a NbN film gated at $V_G = -6$ V, according to XPS survey scan analysis.

VII. MEASUREMENT AND FITTING OF THE TUNNELLING $V(I)$ CURVES

Due to the small thickness and width of the NbN strip, the resistance r_s of the portion of film between the point contact and the V^- contact can be comparable to the resistance of the junction itself. It thus heavily affects the voltage drop measured between the V^+ and the V^- contacts, that turns out to be equal to $V_{\text{exp}}(I) = V(I) + r_s I$. In order to determine the true $V(I)$ we need to eliminate the contribution of r_s . In principle this can be done by carrying out the measurements in the superconducting state; however, the features associated to the energy gap in NbN can disturb the fitting of the $V(I)$ with simple models thought for N/I/N junctions. Therefore, we took the $V_{\text{exp}}(I)$ in the normal state and rescaled the values in such a way that $V(I) = V_{\text{exp}}(I) - r_s I$ is identical to the $V_{\text{exp}}(I)$ curve measured in the superconducting state, apart from the superconducting gap features. This procedure allows determining the value of r_s but, more important, allows constructing the intrinsic current/voltage characteristic of the junction. This curve can be directly compared to the Simmons model in the intermediate voltage range[?], according to which the current flowing through the junction can be expressed as:

$$I = A \frac{e^2}{2\pi h s^2} \left[\left(\phi - \frac{V}{2} \right) e^{-\frac{4\pi s}{h} \sqrt{2me(\phi - \frac{V}{2})}} - \left(\phi + \frac{V}{2} \right) e^{-\frac{4\pi s}{h} \sqrt{2me(\phi + \frac{V}{2})}} \right] \quad (9)$$

where e is the elementary charge, h is the Planck constant, m is the electron mass, A is the junction area, ϕ is the height of the potential barrier and s is the barrier thickness. Thanks to the geometry of our strip, which is 100 μm wide, we were able to estimate that the upper limit for the junction area is $A_{\text{max}} \simeq 1.2 \cdot 10^{-8} \text{ m}^2$ in all our junctions. In order to facilitate the convergence of the fitting procedure, we chose to fix the area at different values (generally from A_{max} down to $0.1A_{\text{max}}$). For each fit, the relative uncertainties of the parameters ϕ and s are very small (in the worst cases, 3% and 1.5%). We then took ϕ and s as the midpoint of the relevant interval of values determined by the fits with different A . The points in Fig.6c and d were obtained in this way, and the error bars correspond to 1/2 of the interval width. In some cases, such uncertainty is smaller than the size of the symbols. Note that the results provide values of ϕ that are larger than the maximum voltage applied through the junction, which justifies the use of the model for the intermediate regime.

-
- [75] A. E. Dane, A. N. McCaughan, D. Zhu, Q. Zhao, C.-S. Kim, N. Calandri, A. Agarwal, F. Bellei, and K. K. Berggren, Bias sputtered NbN and superconducting nanowire devices, *Appl. Phys. Lett.* **111**, 122601 (2017).
 - [76] O. Medeiros, M. Colangelo, I. Charaev, and K. K. Berggren, Measuring thickness in thin NbN films for superconducting devices, *J. Vac. Sci. Technol. A* **37**, 041501 (2019).
 - [1] D. Daghero, F. Paolucci, A. Sola, M. Tortello, G. A. Ummarino, M. Agosto, R. S. Gonnelli, J. R. Nair, and C. Gerbaldi, Large conductance modulation of gold thin films by huge charge injection via electrochemical gating, *Phys. Rev. Lett.* **108**, 066807 (2012).
 - [2] M. Tortello, A. Sola, K. Sharda, F. Paolucci, J. R. Nair, C. Gerbaldi, D. Daghero, and R. S. Gonnelli, Huge field-effect surface charge injection and conductance modulation in metallic thin films by electrochemical gating, *Appl. Surf. Sci.* **269**, 17 (2013).
 - [86] E. Piatti, D. Romanin, R. S. Gonnelli, and D. Daghero, Anomalous screening of an electrostatic field at the surface of niobium nitride, *Appl. Surf. Sci.* **461**, 17 (2018).
 - [10] E. Piatti, D. Daghero, G. A. Ummarino, F. Laviano, J. R. Nair, R. Cristiano, A. Casaburi, C. Portesi, A. Sola, and R. S. Gonnelli, Control of bulk superconductivity in a BCS superconductor by surface charge doping via electrochemical gating, *Phys. Rev. B* **95**, 140501(R) (2017).
 - [82] S. P. Chockalingam, M. Chand, J. Jesudasan, V. Tripathi, and P. Raychaudhuri, Superconducting properties and Hall effect of epitaxial NbN thin films, *Phys. Rev. B* **77**, 214503 (2008).
 - [83] T. S. El-Shazly, W. M. Hassan, S. S. Abd-el Rehim, and N. K. Allam, Optical and electronic properties of niobium oxynitrides with various N/O ratios: insights from first-principles calculations, *J. Photonics Energy* **8**, 026501 (2018).
 - [92] J. G. Simmons, Generalized formula for the electric tunnel effect between similar electrodes separated by a thin insulating film, *J. Appl. Phys.* **34**, 1793 (1963).